Coupled analysis of full flow penetration problems in soft sensitive clays

H. Sabetamal[1], J.P. Carter[2], X. Zhang[3], D. Sheng[1]

[1] School of Civil and Environmental Engineering, University of Technology Sydney, Australia
[2] Priority Research Centre for Geotechnical Science and Engineering, University of Newcastle, Australia
[3] Department of Civil Engineering and Industrial Design, University of Liverpool, UK

Abstract: This study describes the development and implementation of a numerical procedure for the analysis of coupled geotechnical problems involving finite deformations, changing boundary conditions, multiphase porous media and softening behaviour. The numerical scheme is first validated through a benchmark problem concerning the laying of an on-bottom offshore pipeline, and then some further highlights of the effects of soil softening are presented. The scheme is then specifically employed to study the penetration process of a full flow cyclic T-bar test in soft sensitive clay. An advanced soil constitutive model has been implemented to capture the effects of soil structure and its progressive de-structuring as well as soil fabric anisotropy. Accordingly, the changing soil resistance due to the combined effects of soil softening, remoulding and reconsolidation is illustrated, by considering a T-bar undergoing large amplitude cyclic sequences interspersed with consolidation periods. The results from the numerical simulations reveal the effects of soil softening on the soil deformation pattern, the evolution of shear bands, the generation of excess pore pressures and the process of soil reconsolidation.

Keywords: Large deformations, coupled effective stress analysis, T-bar test, finite element method, soil constitutive models.

Introduction

The design of offshore geotechnical projects typically involves an assessment of the undrained shear strength s_u of soft soil that is usually measured by in situ tests, such as the full flow T-bar test (Stewart and Randolph 1991) and free fall (cone or ball) penetrometers (e.g., Nazem et al. 2012; Sabetamal et al. 2016; Sabetamal et al. 2018). A characteristic feature of geotechnical practices related to subsea foundations and anchoring systems concerns the cyclic nature of the applied loading from the ocean environment and operating conditions. The cyclic loading episodes are usually sustained over relatively long periods allowing consolidation to occur. Accordingly, a 'cyclic strength' parameter that can reflect both strength loss and strength recovery (the former due to loss of structure and the latter due to reduction in voids ratio) throughout the remoulding and reconsolidation processes would be useful. However, the effects of reconsolidation on the undrained capacity of offshore structures are usually ignored, whereas the subsequent increase of stiffness and strength of the seabed can significantly affect the fatigue life of structures, such as subsea pipelines, spudcan foundations, steel catenary risers, etc. Therefore, accurate quantification of the soil strength is very important for the sake of safe, economic and realistic design of offshore structures. This requires a careful evaluation of soil behaviour far beyond its initial failure, for which the full-flow T-bar penetrometer test is typically utilised to evaluate the change of soil strength throughout several large amplitude displacement cycles. Hodder et al. (2013) presented such experiments in order to study the behaviour of kaolin clay. Very recently, O'Loughlin et al. (2020) also conducted experiments in order to evaluate the behaviour of carbonate silt and sensitive kaolin clay. Some one-dimensional analytical models predicting the changing soil strength have been presented based on the principles of critical state soil mechanics and observations of soil behaviour during large amplitude cyclic T-bar tests (Hodder et al. 2013; Zhou et al. 2019).

Despite these recent experimental and analytical studies, there is a scarcity of numerical simulations that are capable of capturing the 'whole life' behaviour of subsea foundations and penetration processes involving the correct simulation of in situ stress conditions, generation of excess pore pressures, the loss of soil strength due to soil softening and remoulding effects, as well as soil strength recovery because of soil reconsolidation. The available numerical studies, in particular those concerning penetration of full flow penetrometers, are mainly in the form of undrained analyses with the Tresca material model, which are not able to consider pore pressure generation and dissipation (e.g., Zhu et al. 2020; Han et al. 2020; Zhou and Randolph 2009). A fully coupled analysis is required to incorporate pore-fluid pressure development and its subsequent dissipation. The analysis procedure should also be able to consider large deformation processes, for which a robust mesh optimisation strategy is necessary to circumvent problems associated with severe mesh distortions and the consequential termination of the analyses.

Some recent studies of coupled analysis for deep penetration problems, such as the penetration of a jack-up spudcan (e.g., Wang and Bienen 2016; Rangi et al. 2016), piezocone (Yi et al. 2012) and piezoball (Mahmoodzadeh et al. 2014) are based on the method of Remeshing and Interpolation Technique involving Small Strains (RITSS) proposed by Hu and Randolph (1998), combined with the Modified Cam Clay (MCC) model. They usually consider the relevant structural elements 'wished in place', thus avoiding numerical difficulties associated with their initial surface penetration, so that strictly speaking the 'whole life' behaviour of these applications has not been taken into account. Furthermore, ultra large deformation problems may involve boundary overlapping that cannot be easily handled by the current version of the RITSS method. In addition, these studies have not employed more advanced soil models in order to explicitly incorporate features like soil softening, rate effects and fabric anisotropy.

The natural structure of soft clay formed during geological processes that include cementation, creep and thixotropy, is essentially different from that of clays reconstituted in the laboratory. As a consequence, in situ soft clays generally show stiffer behaviour than laboratory experiments on reconstituted samples, allowing them to exist at a higher void ratio than the equivalent reconstituted samples at a given stress (Burland 1990; Leroueil and Vaughan 1990). Sometimes, the changes in the internal soil fabric under deformation causes a breakdown of the initial structure often resulting in strength loss due to remoulding. This phenomenon is known as de-structuring and can be quite pronounced in natural soft clays (e.g., Callisto and Calabresi 1998; Smith et al. 1992). It is, therefore, important to include the effects of soil structure and the de-structuring process in numerical models when analysing problems involving large deformations and possibly significant soil remoulding.

In this study the development of an effective stress FE procedure is presented that is able to consider all of the aforementioned features in the modelling of large deformation geotechnical problems. Application of the proposed numerical scheme is illustrated through simulation of two challenging geotechnical problems involving an offshore pipe-soil interaction and penetration of a full flow T-bar penetrometer, which undergoes large amplitude cyclic movements after being buried in a soft sensitive saturated clay.

In the following, the FE numerical procedure developed for the study is outlined first, along with a description of the implemented soil constitutive model. The validity of the numerical approach is demonstrated by comparing the results of a pipe-seabed interaction problem with previously published solutions and then the study is further extended to observe the effects of softening on the behaviour of the pipe-seabed system. Finally, numerical simulation of the T-bar penetration process is presented. The numerical results provide some insights into the soil deformation mechanisms, shear band evolution, excess pore pressure generation and the processes of soil structure degradation and reconsolidation.

Numerical procedure

In order to consider large deformation phenomena while avoiding possible mesh distortions, a finite deformation procedure based on the Particle Finite Element Method (PFEM) was developed and implemented into a general-purpose commercial software package, Abaqus. Moreover, an advanced soil constitutive model that can capture soil structure and anisotropy was implemented. A relatively concise description of the numerical framework is presented in the following.

Large deformation FE procedure

To handle large deformation problems, the traditional numerical methods established within a Lagrangian framework are typically replaced by those based on the framework of the Arbitrary Lagrangian Eulerian (ALE) method. Overall, the ALE approaches for geotechnical applications may be divided into three groups: mesh-based methods (e.g., van den Berg 1996; Susila and Hryciw 2003; Nazem et al. 2006); particle based approaches, such as the Material Point Method (MPM) and the Smoothed Particle Hydrodynamics (SPH) method (Sulsky et al. 1995; Beuth et al. 2011; Soga et al. 2016); and the mixed mesh-particle based procedures, such as the PFEM approach (e.g., Idelsohn et al. 2004; Zhang et al. 2019).

The mesh-based ALE schemes used in geotechnical engineering may be divided into three categories: the RITSS procedure (Hu and Randolph 1998), the efficient ALE scheme (EALE) (Nazem et al. 2006) and the Coupled Eulerian-Lagrangian (CEL) approach. Wang et al. (2015) compared the performances of these methods for some benchmark problems covering static, consolidation and dynamic geotechnical applications.

The PFEM that will be adopted in this study is a mixed procedure that considers the meshless definition of a continuum represented by a cloud of particles and then treats the assemblies of those particles with the standard mesh-based FE technique. The notion of a continuum represented by particles allows the possibility of modelling the separation of particles from the main domain or group of particles that may eventually lead to the creation of new surfaces, sub-domains and multibody contacts. The re-entry of particles back into the main domain can also be accommodated.

To date, most of the PFEM-based procedures have been implemented into bespoke codes and their applications are typically limited to some specific problems, such as the modelling of granular flows, landslides, soil-structure interaction, etc. (e.g., Zhang et al. 2013; Monforte et al. 2018). In this study, we have implemented the PFEM approach into the commercial software Abaqus. This has enabled application of the method to a wide range of problems and provides flexibility by providing access to its numerous capabilities, including user-defined subroutines.

PFEM analysis strategy

The starting point at each time step of a PFEM analysis involves a cloud of particles C^n specified to form the analysis domain(s) at time t_n, as depicted in Figure 1. The boundaries defining the domain are then identified by coupling the *Delaunay* triangulation of those particles with the so called *α-shape* method (Edelsbrunner 1994). Subsequently, the discretisation of the continuum is performed with a FE mesh M^n and the corresponding Lagrangian equations of motion are solved. For the next time step, the mesh nodes at their new positions are considered to be the updated cloud of particles C^{n+1}, for which the solution process is then repeated, accordingly. As the analysis proceeds, particles may concentrate at some regions and subsequently the number of particles would decrease in other regions, eventually leading to a loss of solution accuracy. In order to preserve the quality of the mesh, some particles may be merged or added depending on their separation. The insertion of particles is considered for elements for which their corresponding area exceeds a specified tolerance; and particles that are closer than a characteristic distance are removed. The process of insertion and removal of particles follows the algorithm described in Chargoy (2014). Moreover, a Laplacian smoothing is performed for some selected regions in order to smooth elements with unacceptable aspect ratios. Finally, having completed the mesh refinement process, the mapping of all Gauss and nodal variables from the old mesh to the new (refined) mesh is performed by interpolating results from nodes in the old mesh to points (either nodes or integration points) in the new mesh. To compute nodal stresses and state parameters, the super convergent patch recovery technique is used (Zienkiewicz and Zhu 1992).

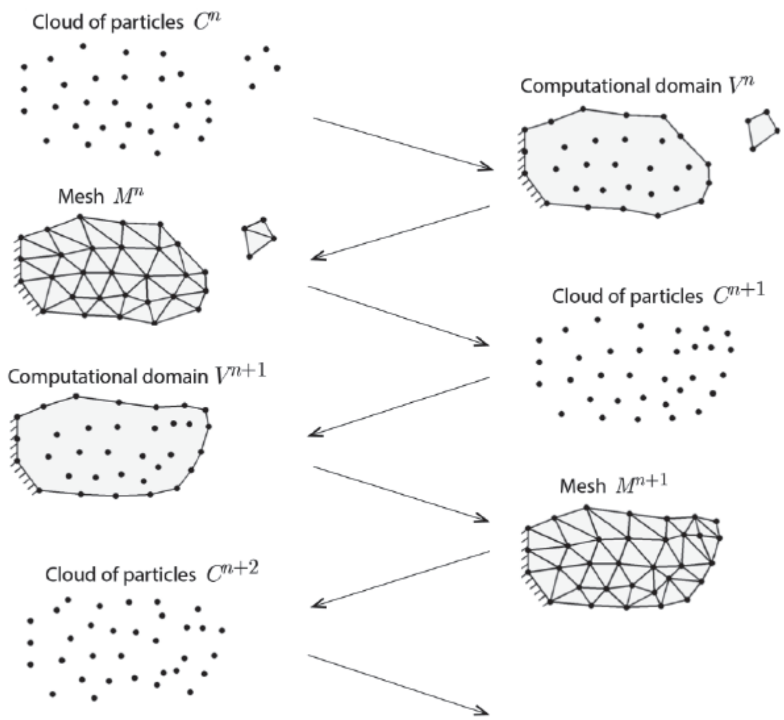

Figure 1. PFEM analysis procedure (after Zhang et al. 2013)

It is noteworthy that the external boundaries generated through the *α-shape* method may violate the mass conservation of the continuum depending on the value chosen for the parameter α. This can be avoided by the use of a constrained *Delaunay* algorithm, such as the one described in Rodriguez et al. (2015). This study employs a relatively similar approach in which the old boundary is refined by adding some virtual particles to it prior to performing the *Delaunay* triangulation process. The corresponding so-called constrained *Delaunay* approach is less sensitive to the value of the *α-shape* parameter so that the boundary is identified accurately. Once the domain boundaries are recognised, the virtual particles are eliminated and the solution process is continued.

It is noteworthy that the PFEM has some similarity with the RITSS method in terms of the repeated interpolation and remeshing (or mesh refinement) processes, but the main difference is in the capability of PFEM in identifying free surfaces that may involve possible formation of new surfaces, boundary merging and multibody contacts.

Soil constitutive model

The constitutive model (or models) perform a major role in the analysis of any boundary value problem, usually providing the connection between imposed stresses and the resulting strains. The Modified Cam Clay (MCC) model is an isotropic critical state soil model and is now widely used for predicting soil behaviour. The model has been the subject of significant research since its inception and modified in various forms to cover different soil types and loading conditions in an attempt to achieve better predictions of experimental data. A number of extensions to this model have been proposed to capture the directional bias of the soil response due to the orientation of soil fabric. This includes the development of anisotropic constitutive models, such as SANICLAY (Dafalias 2006) and S-CLAY1 (Wheeler et al. 2003). A few other extensions introduced a measure of the material structure into the MCC model with the so-called structured Cam-clay models (e.g., Liu and Carter 2002; Yang et al. 2016). Similarly, a de-structuring theory was applied to the S-CLAY1 (Karstunen et al. 2005) and the SANICLAY (Taiebat and Dafalias 2010) models to account for bonding and de-structuring effects. The structured S-CLAY1 that was named S-CLAY1S involves isotropic de-structuring, only, while the SANICLAY model considers both isotropic and deviatoric de-structuring.

In this study, we have implemented S-CLAY1S as an anisotropic structured model. Note that the structure/de-structuring effects incorporated herein include softening effects, in which the undrained shear strength may decrease with increasing plastic deformation. This is analogous to the strategy adopted in some undrained analyses using the Tresca model, where the undrained shear strength is treated as a function of accumulated plastic shear strain (e.g., Einav and Randolph, 2006).

Yield and plastic potential functions

Assuming an associated flow rule, the S-CLAY1S model employs a rotated and distorted ellipse (in triaxial stress space) to describe both the plastic potential and yield surfaces (Figure 2), which in the general stress space is given as

$$f = \frac{3}{2}(\mathbf{s} - p'\boldsymbol{\alpha}):(\mathbf{s} - p'\boldsymbol{\alpha}) - \left(M^2 - \frac{3}{2}\boldsymbol{\alpha}:\boldsymbol{\alpha}\right)p'(p_c - p') = 0 \tag{1.1}$$

where $\mathbf{s} = \boldsymbol{\sigma} - p'\mathbf{I}$ is the deviatoric stress, $\boldsymbol{\sigma}$ and $\mathbf{I}$ are, respectively, the effective stress tensor and identity tensor, p' denotes the mean effective stress, M is the critical stress ratio for triaxial compression, p_c represents the internal hardening parameter controlling the size of the yield surface and $\boldsymbol{\alpha}$ denotes the evolving deviatoric stress-ratio (backstress) tensor, which is the kinematic hardening parameter of the model. Moreover, the model was extended to include a dependency on the third invariant of stress via the Lode angle (Figure 2b). This was attained by assuming that the plastic potential surface has a noncircular but smooth shape in the deviatoric plane which coincides with the Mohr-Coulomb hexagon at all vertices (e.g., see Sheng et al. 2000).

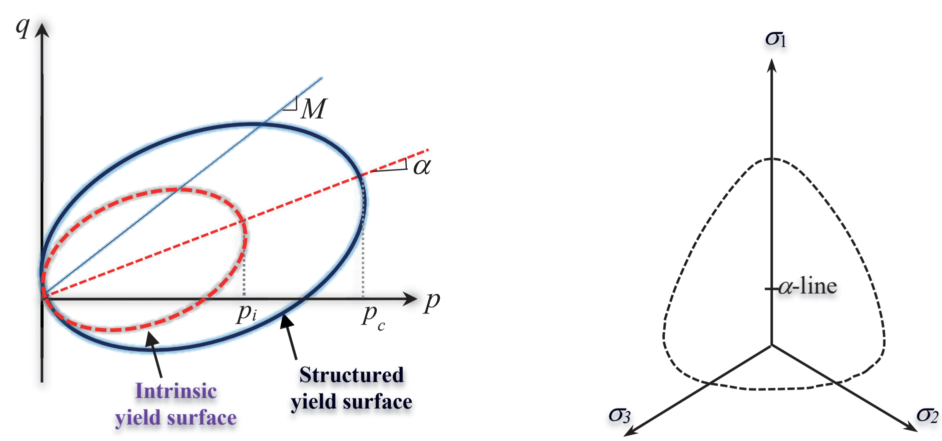

(a) (b)

Figure 2. S-CLAY1S model in: (a) triaxial stress space (p: mean effective stress; q: deviatoric shear stress); (b) deviatoric plane

Soil structure effect

Following the concept proposed by Gens and Nova (1993), the effect of bonding in the model was implemented by introducing an intrinsic (reconstituted) yield surface that has the same shape and inclination as the natural (structured) yield surface but with a smaller size, as shown in Figure 2a. The size of the intrinsic yield surface is specified by parameter p_i which is related to the size of the natural yield surface p_c as

$$p_c = p_i\left(1+\chi\right) = p_i S_t \tag{2}$$

where χ denotes the current amount of bonding and $S_t = (1+\chi)$ is referred to here as the soil sensitivity parameter. Expansion or contraction of the intrinsic yield surface is controlled by the plastic volumetric increment $d\varepsilon_v^p$ according to the isotropic hardening law of the MCC model, as

$$dp_i = \frac{v p_i}{\lambda_i - \kappa} d\varepsilon_v^p \tag{3}$$

where v is the specific volume, λ_i is the gradient of the intrinsic normal compression line in the v–ln(p') plane and κ denotes the slope of the swelling line in the same plane.

The isotropic de-structuring law for this model (Karstunen et al. 2005) describes the degradation of the bonding parameter χ based on a combination of the incremental plastic volumetric strain $d\varepsilon_v^p$ and the plastic deviatoric strain $d\boldsymbol{\varepsilon}_d^p$ as

$$d\chi = -a\chi\left[\left|d\varepsilon_v^p\right| + b\left|d\boldsymbol{\varepsilon}_d^p\right|\right] \tag{4}$$

where parameter a controls the absolute rate of isotropic de-structuring and parameter b defines the relative effectiveness of deviatoric and volumetric plastic strains in degrading the interparticle bonding. Note that the structure degradation is a function of the incremental plastic strains instead of the accumulated plastic shear strain, which is commonly used to account for softening effects with the Tresca model (Einav and Randolph, 2006). Avoiding the use of accumulated plastic strain could be regarded as an advantage when the analysis involves repeated processes of remeshing and interpolation, because the mapping of accumulated plastic strains is no longer required. The latter usually involves some form of error growth leading to gradual smoothing of the plastic strain distribution.

Volumetric collapse occurs during the de-structuring process and the natural yield surface begins to shrink towards the fully remoulded (intrinsic) yield surface. Once the natural yield surface coincides with that of a soil in the reconstituted state, the structure is completely removed and the intrinsic state of a reconstituted soil is eventually obtained.

Kinematic hardening

The evolution of the backstress ratio tensor is controlled by the particular form of the hardening law (Wheeler et al., 2003) as

$$d\boldsymbol{\alpha} = C_\alpha \left[\left(\frac{3}{4} \frac{\mathbf{s}}{p'} - \boldsymbol{\alpha} \right) \left\langle d\varepsilon_v^p \right\rangle + x_\alpha \left(\frac{1}{3} \frac{\mathbf{s}}{p'} - \boldsymbol{\alpha} \right) \left| d\boldsymbol{\varepsilon}_d^p \right| \right] \tag{5}$$

where $\langle (\cdot) \rangle$ is the step function of $(\cdot)$ defined as

$$\left\langle \dot{\varepsilon}_v^p \right\rangle = \dot{\varepsilon}_v^p \quad \text{if} \quad \dot{\varepsilon}_v^p > 0 \qquad \text{and} \qquad \left\langle \dot{\varepsilon}_v^p \right\rangle = 0 \quad \text{if} \quad \dot{\varepsilon}_v^p \le 0 \tag{6}$$

The material constant x_α controls the relative contribution from the volumetric and deviatoric plastic strains and C_α scales the absolute rate of evolution.

Numerical integration of constitutive relations

Integration of the stress-strain laws is typically performed using either explicit or implicit schemes. It may be argued that the implicit schemes are more accurate than simple explicit approaches, as the latter involve some errors due to the approximate satisfaction of the yield and consistency conditions. However, the use of implicit schemes, such as the 'backward Euler return mapping' with complex models becomes very cumbersome mainly because of the need to compute the second-order derivatives of the plastic potential and also the difficulty in deriving a consistent tangent operator. Therefore, it is likely that explicit schemes would be more favourable for complex constitutive soil models provided their accuracy and efficiency are enhanced through automatic sub-incrementing and error control strategies. Therefore, for the purpose of this study, the soil model was implemented through a UMAT subroutine into the Abaqus software based on the adaptive substepping scheme of Sloan et al. (2001). For the results presented in this paper, the constitutive laws were integrated very accurately by using a relative error tolerance of 10^{-6} for the stresses, together with an absolute tolerance of 10^{-9} for drift from the yield surface.

Validation and numerical applications

The numerical scheme developed in this study was employed to simulate two challenging problems of offshore geomechanics. First, the analysis of a partially embedded pipeline is presented and the results are compared to the solutions presented earlier by Chatterjee et al. (2013). This is followed by an extended study on the effects of soil softening on the pipe response. The second example concerns the simulation of a full flow cyclic T-bar test.

Pipe seabed interaction

In this simulation, a rigid pipe of diameter D was laid on a saturated soil and pushed vertically to an embedment depth of $0.5D$ by applying prescribed displacements. Advantage was taken of the problem's symmetry and only one-half of the model was represented in the numerical simulation. A two-dimensional plane strain FE model discretised through 6-noded, coupled triangular elements comprising three Gauss points was adopted for the numerical analysis, as depicted in Figure 3.

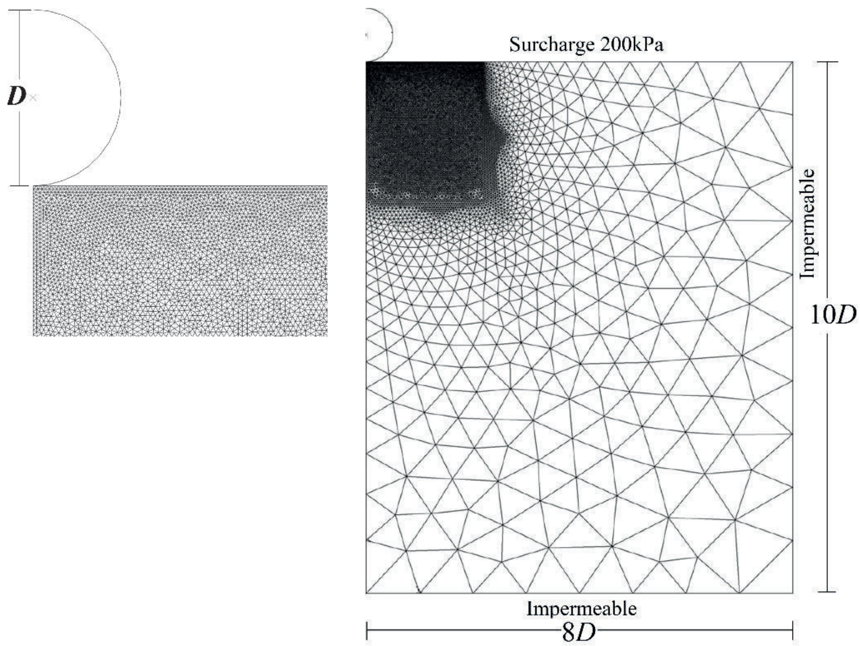

Figure 3. FE model for the pipe-seabed interaction

The side boundaries of the FE model were restrained against horizontal movement, while the bottom boundary was fixed, preventing both vertical and horizontal movement. Drainage was permitted only on the top boundary and pore-water flow normal to the pipe-soil interface was prohibited.

The pipe-soil interface was assumed to be smooth and a uniform pressure of 200 kPa was applied at the mudline in accordance with the simulations presented in Chatterjee et al. (2013). Moreover, the S-CLAY1S model implemented in this study was employed to predict the soil behaviour. The values of the soil parameters adopted for the constitutive model are listed in Table 1, in which basic (critical state) soil parameters are typical of the kaolin clay determined through laboratory element tests at the University of Western Australia (Stewart, 1992). Furthermore, the soil anisotropy and structure parameters used in the model were chosen based on the suggestions by Yin et al. (2010). Note that setting the anisotropy and structure parameters to zero retrieves the MCC model that is referred to here as non-sensitive clay. In the latter case, the predicted results are compared to the results obtained by Chatterjee et al. (2013) for the purpose of validation.

Table 1. Soil model parameter values

Basic parameters	Value
Friction angle	$\phi' = 23°$
Stress ratio at critical state	$M = 0.898$
Slope of normally consolidated line in *e-ln(p')* space	$\lambda_i = 0.205$
Slope of unloading-reloading line in *e-ln(p')* space	$\kappa = 0.044$
Void ratio at p'=1 kPa on critical state line	$e_{cs} = 2.14$
Over consolidation ratio	$OCR = 1$
Poisson's ratio	$\upsilon' = 0.3$
Saturated bulk unit weight	$\gamma_{sat} = 15$ kN/m^3
Unit weight of water	$\gamma_w = 10$ kN/m^3
Permeability of soil	$k = 1\times10^{-9}$ m/s
Structure parameters	$\chi = 0, 4, 9$
	$a = 0.2$
	$b = 9.0$
Anisotropy parameters	$C_\alpha = 50$
	$x_\alpha = 1$
	$\alpha_0 = 0.59^*$

* Note that α_0 is the scalar value of initial anisotropy $\boldsymbol{\alpha}_0$ as $\alpha_0 = 3/2(\boldsymbol{\alpha}_0 : \boldsymbol{\alpha}_0)$

A fine mesh with minimum size of 0.02D was applied near the pipe extending up to 2.25D from the centreline and 2.6D below from the mudline. The development of shear bands in strain-softening material can lead to solution non-uniqueness (Zienkiewicz and Taylor, 2000) because the FE discretisation effectively imposes an artificial internal length parameter. This can affect both the thickness and orientation of the predicted shear band. In general, the shear band thickness usually takes the minimum size possible. In these cases, some regularisation techniques might be used to circumvent this difficulty, by introducing length scales in the formulation (e.g., by using gradient-dependent plasticity, nonlocal plasticity and enhanced microstructure continua), with which a realistic shear band thickness could be predicted (e.g., Collin et al. 2006; De Borst et al. 1993). In coupled analyses involving soft sensitive clays, it seems that the mesh dependency of the solution may not be as severe as in a single phase material, largely because the generation and dissipation of pore pressure in shear bands may regularise the strain softening (e.g., Thakur, 2018). Shuttle and Smith (1990) suggested that pore water pressure migration in relation to shear band formation is more critical in numerical modellings rather than the width of rupture bands. Nonetheless, the problem of solution non-uniqueness was avoided in this study by adopting an element size around the penetrometer

(~0.02D) that is representative of the typical shear band thickness (0.1 mm to 2 cm) observed for soft sensitive clays (e.g., Lin and Penumadu 2006; Moore and Rowe 1988). It is noteworthy that in another attempt we increased the density of mesh by halving the element sizes (~0.01D) which did not significantly affected the predictions and the observed soil-pipe response.

Two different pipe penetration velocities, v, were considered to represent undrained and partially drained situations for which the corresponding values of the dimensionless velocity vD/c_v were chosen as 100 and 0.1, respectively. The coefficient of consolidation c_v was determined from

$$c_v = \frac{k}{m_v \gamma_w} \tag{7}$$

where m_v is the volume compressibility of the solid soil skeleton. The virgin compressibility in the *Cam Clay* model can be expressed as

$$m_v = \frac{\lambda}{\left(1+e_0\right) p'_0} \tag{8}$$

where p'_0 and e_0 denote the initial mean effective stress and void ratio at the pipe invert, respectively.

Figure 4 depicts the profile of penetration resistance V normalised by the undrained shear strength s_{u0} at the pipe invert (s_{u0} = 57.2 kPa), obtained from the MCC parameters for one-dimensionally (K_0 = 1-sinϕ = 0.61) consolidated soil (e.g., see Wroth 1984). Figure 4 shows that the soil resistance increases with penetration depth w and is higher for the slow penetration case (vD/c_v = 0.1). The profile of soil resistance for the fast penetration case of the insensitive clay (vD/c_v = 100) is comparable with the result of an equivalent uncoupled analysis using the Tresca soil model, assuming the same initial undrained shear strength profile. Therefore, the coupled analysis actually predicts the undrained behaviour for the case of a high penetration velocity. The numerical results are also compared with those of Chatterjee et al. (2013), showing excellent agreement.

Figure 4 also depicts the predicted results for fast penetration into two different sensitive clays with values of the sensitivity parameter S_t = 2 & 10. The penetration resistance for these cases lies below that obtained for the insensitive clay. Note that the penetration resistance was normalised based on the initial intact undrained shear strength (s_{u0}) at the soil surface.

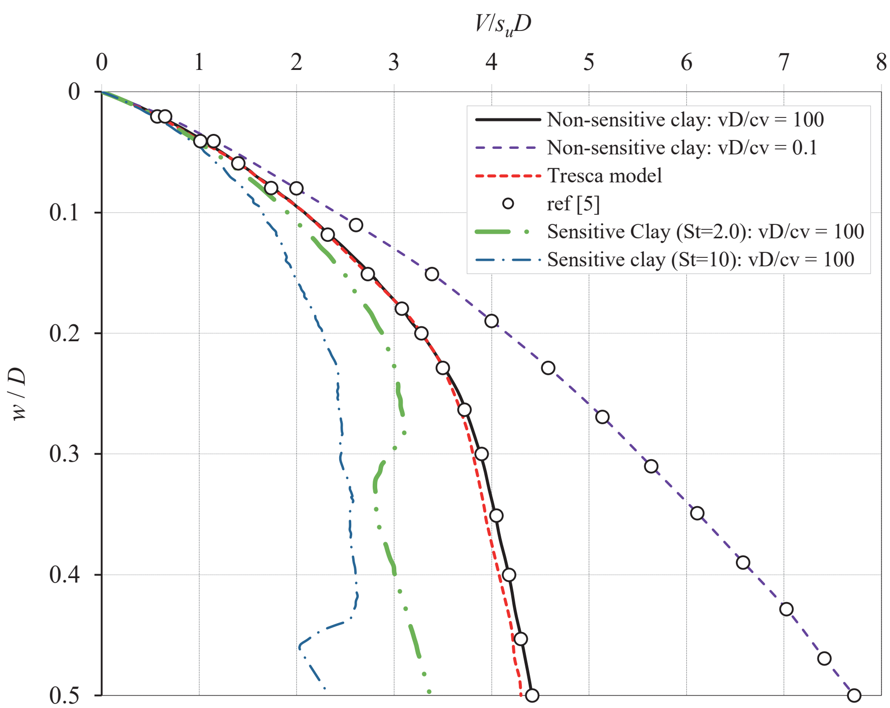

Figure 4. Soil resistance profile

The sudden drop of the soil resistance in the sensitive clays at various penetration depths indicates the development of shear slip surfaces, as will be discussed in the following.

Figure 5 presents some contour plots of the accumulated plastic shear strain at the final embedment depth. The localization of plastic deformation into narrow bands, referred to as shear bands, appears to be distinctly different for the sensitive clays compared to the insensitive soil (c.f., Figs 5a & c). Multiple localised zones are formed in the sensitive soil and propagate deeper due to soil softening, whereas for the case of an insensitive clay, plastic shear strains essentially remain uniform and diffused (Fig 5c). The non-uniform distribution of plastic strain in sensitive clays leads to the development of a progressive failure mechanism. At certain penetration depths, the nets of wedge-shaped shear bands, which are locally developed under the pipe, begin to join together through a main curvilinear slip surface that eventually intersects the soil surface. At this stage, which may be considered as the onset of a global failure mechanism, the soil resistance experiences a sudden decrease due to sliding of the soil mass along the slip surface. The slip surfaces developed in the soil are clearly visible in Figures 5a & b. The penetration depth at which the last slide occurs is deeper in the highly sensitive clay (w=0.45D) compared to the less sensitive case (S_t = 2), which happens at around w=0.3D and is also identifiable in Figure 4 as a distinct drop in the soil resistance. This is because the localised shear zones in the highly sensitive clay tend to propagate deeper and thus involve a larger soil mass, delaying the formation of subsequent slip surfaces.

The accumulation of deviatoric plastic strains in the shear bands softens the surrounding soil and progressively breaks down the soil structure. Such disturbance can lead to significant changes in the operative shear strength (Figure 4) and the basic constitutive properties of the soil.

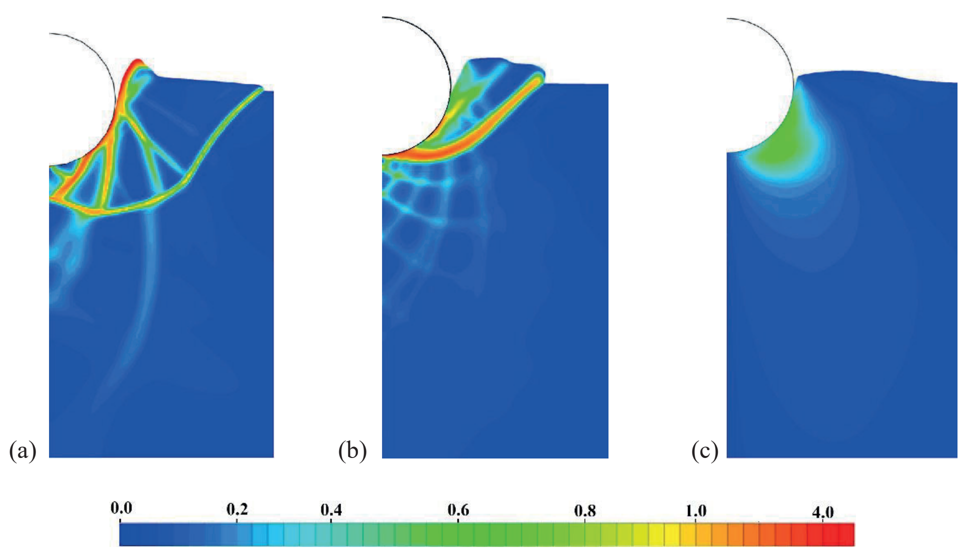

Figure 5. Contour plots of accumulated plastic shear strain at the final embedment depth (w/D=0.5): (a) S_t = 10; (b) S_t = 2.0; (c) *non-softening*

The degradation of soil strength has been visualised through contour plots of the structure parameter χ in Figure 6. The red colour in these plots indicates the (elastic) regions with no softening (intact soil) while the blue regions represent the fully remoulded situation. The observed marked difference in the evolution of shear bands for the different cases should also have significant consequences in terms of the excess pore pressure development, as is illustrated in Figure 7.

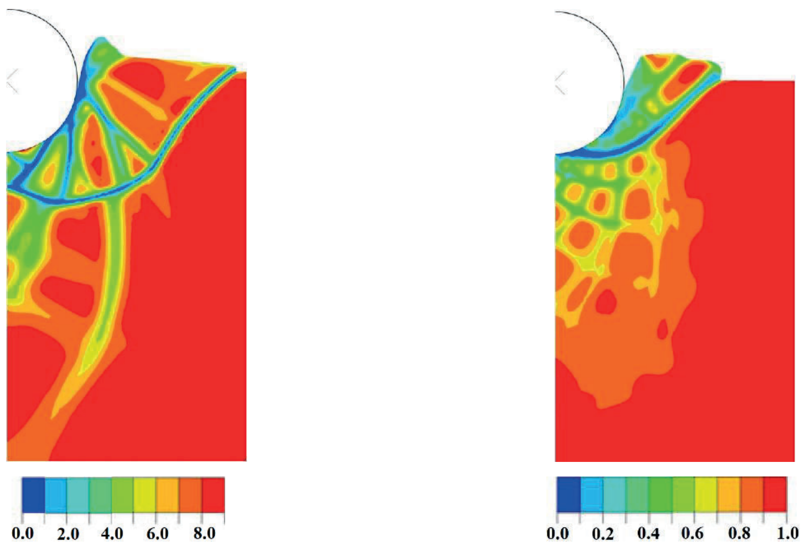

Figure 6. Contour plot of soil structure parameter (χ): (a) $\chi = 9.0$ (S_t=10); (b) χ =1.0 (S_t =2)

The maximum excess pore pressure value is initially observed at a point in contact with the pipe invert for all cases. The uniform shape of the contours for the insensitive case (Figure 7a) is analogous to the uniformly curved surface geometry of the pipe and also the distribution of plastic strains (Figure 5c). The extent of the compressive pore pressure contours indicates the amount of soil undergoing compression and shearing because of the pipe loading. Figures 7b & c show that the excess pore pressures are generally localised within the shear bands in the sensitive clays and they drastically alter the shape of excess pore pressure distributions causing lateral shrinkage of the contours.

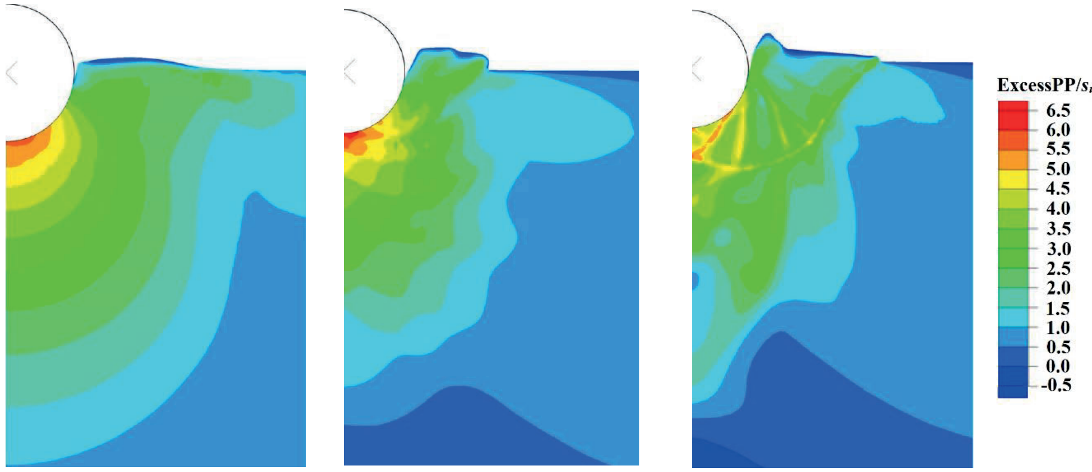

(a) (b) (c)

Figure 7. Excess pore pressure contour plots (normalised by s_{u0}): (a) *non-softening*; (b) $S_t = 2$; (c) $S_t = 10$

The dissipation of excess pore pressures generated throughout the penetration process will lead to consolidation displacements. To study the consolidation process, the excess pore pressures were allowed to dissipate under constant pipe load. The value of this load was that experienced at the final embedment depth. Figure 8 shows the variation of consolidation settlement of the pipe Δw with dimensionless time factor $T_v = c_v t/D^2$, where t denotes the actual time. For the non-sensitive case, the analysis results are also compared with the results given in Chatterjee et al. (2013), showing good agreement between the results and thus providing further validity of the numerical approach.

For the softening cases, sections of the soil mass under the pipe slide along the activated slip surfaces (shear bands) because of the sustained applied load, which leads to an immediate pipe penetration. During this stage, further shear bands are progressively developed in order to build up the overall soil resistance, after which the dissipation of excess pore pressures takes place. Figure 8 illustrates this process, which for the cases where $S_t = 2$ and $S_t = 10$, the initial pipe penetration increases to approximately $0.5D$ and $0.4D$, respectively, over a dimensionless time interval up to $T_v = 1.0\text{e-}12$. The pore pressure dissipation process then becomes noticeable at around $T_v = 0.035$ and finishes at approximately $T_v = 70$ and $T_v = 100$ for the less and more highly sensitive cases, respectively, resulting in corresponding consolidation settlements of approximately 0.2D and 0.22D. Note that for the less sensitive case the dissipation process is shorter (T_v = 70) compared to the highly sensitive case (T_v = 100), probably because of the localisation of excess pore pressures in multiple shear bands that intersect the free draining soil surface (Figure 5b and Figure 9b-top) in the less sensitive case. In the highly sensitive case the shear bands tend to propagate deeper in the soil.

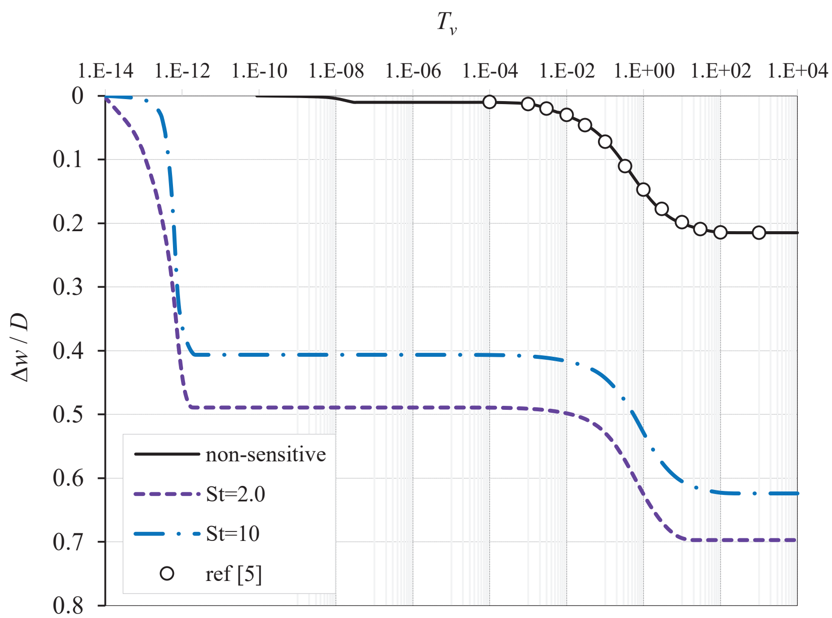

Figure 8. Consolidation settlements versus dimensionless time factor T_v

As can be seen in Figure 8, the amount of immediate penetration is larger in the soil with S_t = 2 compared to the case with S_t = 10. This may not be surprising because of the different soil deformation patterns and the developed shear bands, as observed in Figure 5. A larger part of the soil mass remained elastic (intact) in the highly sensitive clay at the end of pipe embedment compared to the less sensitive clay. Furthermore, the value of applied consolidation load, which was equal to the load experienced at the end of initial (undrained) embedment, was larger for the case with S_t = 2 (V/s_uD=3.37) compared to the case with S_t = 10 (V/s_uD=2.33).

To conclude this example, the build-up of soil strength due to the reconsolidation process is presented by visualising the change of soil hardening parameter p_c. Figure 9 depicts these plots at three stages corresponding to non-dimensional time factors of T_v = 0.0, 0.035 and 100. The immediate penetration stages finish at T_v = 0.035 and the dissipation of excess pore pressures begins thereafter. During the process of immediate penetration, the zones of localisation of shear stresses continue to spread outside the previously developed slip surface in the case of the less sensitive soil (Figure 9b-top). Whereas in the case of the highly sensitive soil, further plastic deformation appears to remain within the section of soil between the pipe and the active slip surface first developed (Figure 9b-bottom).

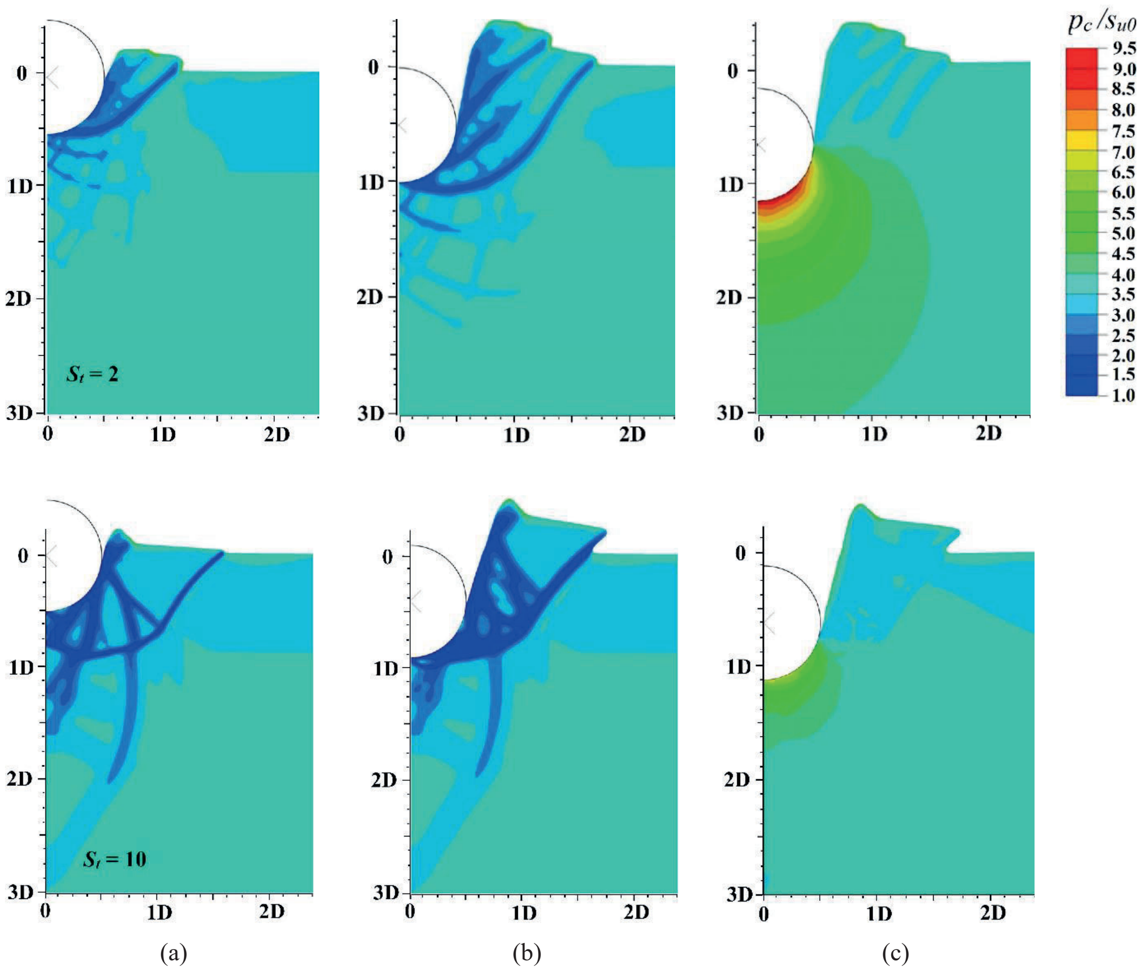

Figure 9. Contour plots of the soil hardening parameter p_c: (a) T_v = 0.0; (b) T_v = 0.035; (c) T_v = 100 (S_t=10 bottom row; S_t =2 top row)

Simulation of full flow T-bar penetrometer

In this example simulation of a rigid T-bar of diameter D continuously penetrated into a soil layer by applying prescribed displacements is presented. Due to symmetry only one-half of the model was represented in the numerical simulation, as depicted in Figure 10. Similar to the previous example, the soil domain was discretised using 6-noded plane strain triangular elements involving three Gauss points. The minimum size of the smallest elements surrounding the surface of the penetrometer was taken as $0.02D$ and the element size increased gradually towards the domain boundaries.

The bottom boundary was fixed in both the horizontal and vertical directions while the lateral boundaries were only fixed in the horizontal direction. Moreover, all boundaries were considered undrained during the penetration process and only the top boundary was changed to the drained condition throughout the consolidation phase. A nominal surcharge of 2 kPa was applied initially at the mudline to avoid numerical difficulties due to zero mean effective stress. The interface between soil and the T-bar was assumed to be frictionless because low permeability of the soil effectively imposes undrained conditions and so there would not be significant tangential stresses at the interface.

The T-bar was first penetrated at a constant rate from the soil surface to a target depth of $9.4D$, followed by large amplitude cyclic sequences, undertaken with displacement control, interspersed with consolidation periods, during which the T-bar was held at a fixed position. The displacement-controlled cycles involved moving the T-bar vertically up and down repeatedly over a range of $4D$ for N = 3.5 cycles in episode 1 and N = 2 cycles in episode 2 (Fig. 10a). The target depth of $9.4D$ provided enough clearance between the mesh boundaries and the lower and upper apex of the T-bar, before proceeding to the cyclic sequences. It also enabled observation of pore pressure generation and dissipation patterns at shallow and deep penetration depths. The cyclic displacement range ($4D$) was large enough to avoid overlapping between the flow mechanisms at the midpoint of the cyclic range and at the highest (or lowest) position. Zhou and Randolph (2009) recommended a minimum cyclic range of $3D$ to avoid overlapping flow mechanisms and this was also supported by field evidence in highly sensitive clays, suggesting ranges exceeding about one diameter to be sufficient (Yafrate et al., 2009).

The soil constitutive parameters adopted in this problem are the same as those used in the previous example except that the soil sensitivity parameter was considered as $S_t = 5$ and the soil fabric anisotropy was switched off.

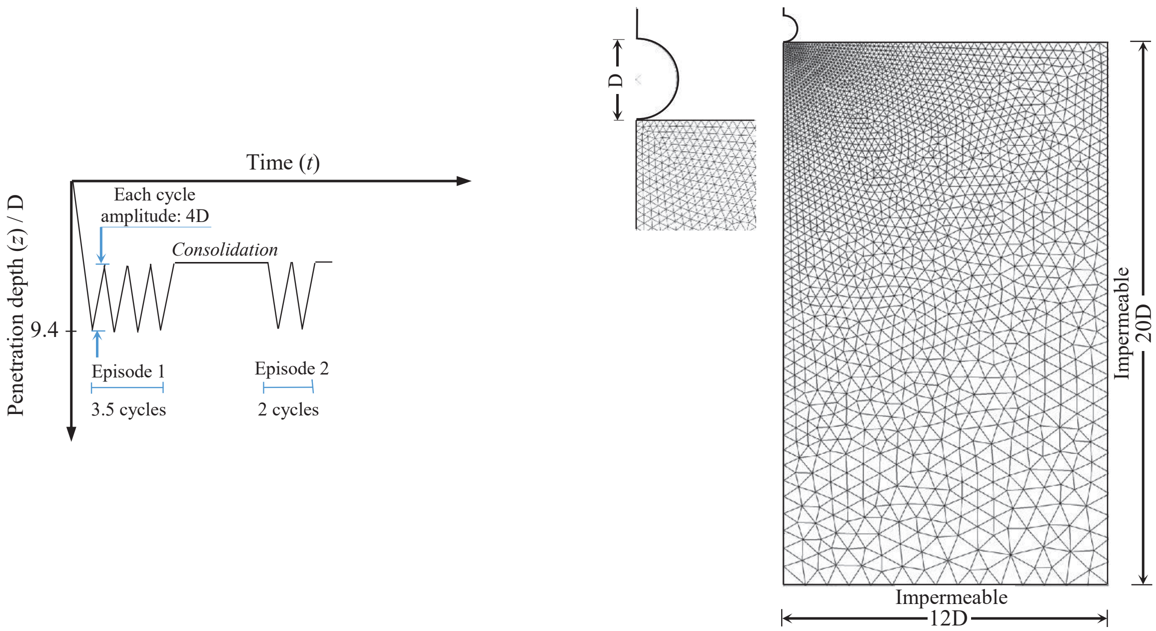

(a) (b)

Figure 10. (a) T-bar simulation process; and (b) FE model adopted for the simulation

Soil resistance and deformation pattern

For the adopted soil parameters, the initial undrained shear strength in plane strain is calculated as $s_{u0} = 0.8+2z$, where z is the depth from the soil surface in metres. Herein we assume that s_{u0} is the initial intact (*structured*) shear strength independent of the assumed bonding parameter χ. In reality, soils with more bonding should have higher (intact) undrained shear strengths.

Nevertheless, because the value of s_{u0} increases with depth, the soil penetration resistance also continues to increase with the penetration depth (Figure 11a) and does not converge to a steady value, as observed in some field and centrifuge T-bar tests (e.g., Hodder et al. 2013).

However, if the soil resistance is normalised by the undrained shear strength at the corresponding penetration depth, a steady normalised soil resistance is eventually obtained, as shown in Figure 11b. The intact initial undrained shear strength corresponding to the lower apex of the T-bar was used for the normalisation of soil resistance in Figure 11b. It is noted that the steady state value is achieved at a shallower penetration depth in sensitive clay (1.1D) compared to the non-softening case attained at approximately 1.95*D*.

Sometimes the deep failure mechanism is associated with steady soil resistance (White et al. 2010), which might be achieved theoretically if a uniform shear strength is assumed for the entire soil profile. The link between the deep failure mechanism and steady *normalised* soil resistance was actually observed in this analysis. Figures 12 and 13 show that the depth at which the failure mechanism changes from surface heave to a deep (flow-round) mechanism is shallower in the sensitive clay (w/D = 1.1) than the non-sensitive case (w/D = 1.95). These transition depths correspond to the situations where the normalised soil resistance converges to a steady value (Figure 11b) and the full diameter of the T-bar comes into contact with the soil (Figures 12c & 13c).

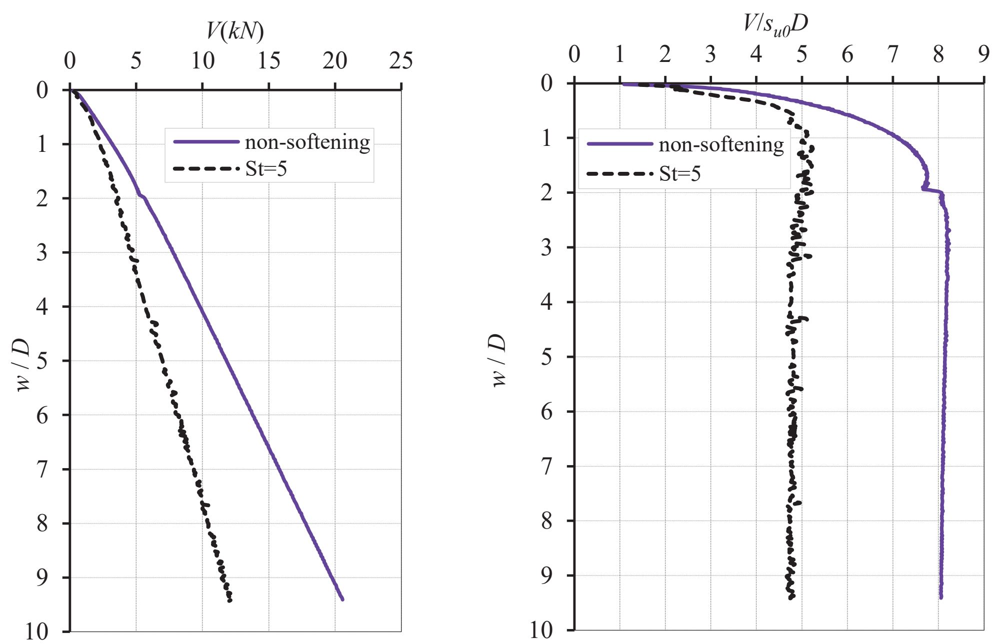

Figure 11. (a) Soil resistance profile (kN); (b) Normalised soil resistance profile

The soil deformation pattern and the developed shear bands are depicted in Figures 12 & 13 for the sensitive and non-sensitive cases, respectively. A curvilinear shear band is initially formed ahead of the advancing T-bar and extends to the soil surface, representing the shallow failure mechanism (Figures 12a & b and 13a & b). Rapid softening of the material close to the T-bar provides a significantly compact failure mechanism in sensitive soil compared to a non-softening soil. The width of the mechanisms for each case are approximately 0.90D and 1.5D, respectively, as measured from the centreline. Once the first shear band intersects the soil surface, another distinct localised shear zone is formed around the T-bar which continues to grow with further penetration and eventually intersects the soil surface (Figures 12b & 13b). Consequently, the soil flows around and over the T-bar leading to a deep failure mechanism, in which soil backfilling and complete burial of the T-bar occur. This happens at the penetration depth of w/D = 1.1 in the sensitive soil case, with no creation of a trapped cavity (Figure 12c), whereas in the case of an insensitive soil a deep mechanism occurs at an embedment depth of w/D = 1.95 (Figure 13c) and it contains a trapped cavity. The larger dimension of the initial soil failure mechanism above the T-bar in the latter case compared to the former case led to the creation of the trapped cavity. It could be sustained because of the suction pore pressure changes and the nonzero undrained shear strength predicted by the constitutive model. Furthermore, the generation of suction in the soil surrounding the trapped cavity marginally increases the undrained shear strength which then prevented the shear band from intersecting the boundary of the trapped cavity (Figure 13d) so that it could remain stable during the analysis process.

Peuchen and Terwindt (2016) noted the significance of the partial flow of soil on the interpretation of in situ T-bar measurements. They also noted that the length of the zone with a trapped cavity depends on the soil strength and over-consolidation ratio; it may exceed 1.0 m for standard miniature T-bars.

The creation of a trapped cavity was also observed by Tho et al. (2012) and Wang et al. (2020), suggesting that its formation and evolution depend on the value of the normalised undrained shear strength parameter ($s_u/\gamma' D$). Through some centrifuge tests and numerical analyses of T-bar, Wang et al. (2020) showed that for uniform clay deposits with $s_u/\gamma' D \leq 1$, the span of a trapped cavity is negligible and thus a flow-round (deep) failure mechanism directly follows the initial (shallow) failure mechanism; for deposits with $1 < s_u/\gamma' D \leq 8.3$, a trapped cavity is created and then closes at further penetration; whereas for $s_u/\gamma' D > 8.3$ closure of the trapped cavity does not occur. The value of the initial undrained shear strength in this study ($s_{u0} = 0.8+2z$) implies that the value of the undrained shear strength at the lower apex of the T-bar satisfies the criterion $s_u/\gamma' D \leq 1$ up to a penetration depth of $0.2D$ for the non-sensitive case, suggesting that a cavity should be created. However, for the sensitive case, the corresponding depth range satisfying the above criteria is proportionately larger because of the rapid soil softening and loss of soil structure around the T-bar. In this case soil backflow, which is quite shallow and contained in that depth range of interest, should not produce a trapped cavity.

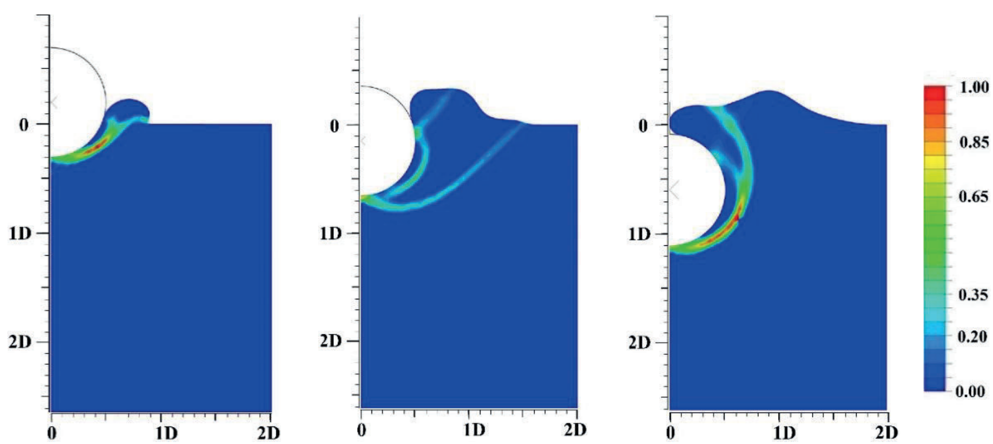

(a) (b) (c)

Figure 12. Soil deformation pattern in sensitive clay: (a) & (b) shallow failure mechanism; (c) deep failure mechanism (the scale represents incremental shear strain)

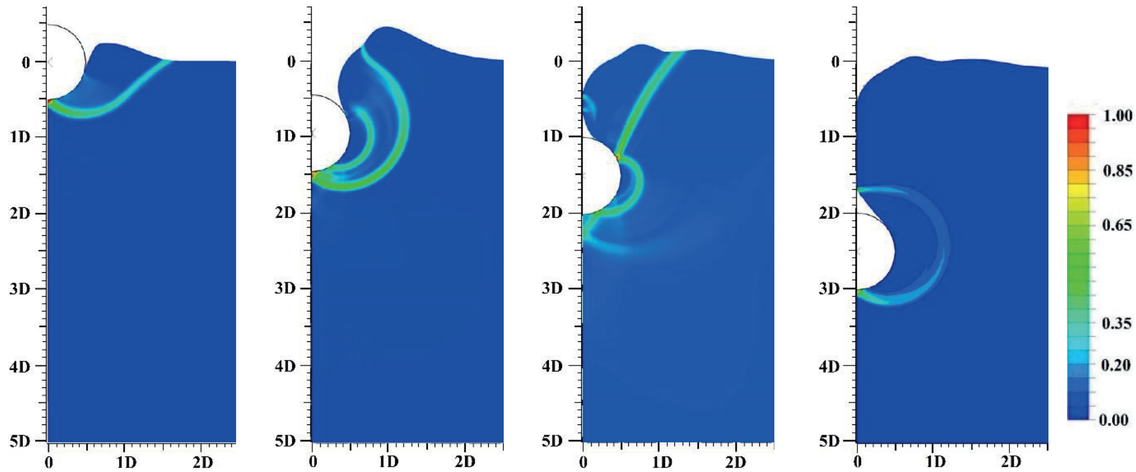

(a) (b) (c) (d)

Figure 13. Soil deformation pattern in non-sensitive clay: (a) & (b) shallow failure mechanism; (c) & (d) deep failure mechanism with trapped cavity (the scale represents incremental shear strain).

Soil softening and degradation during cycling

The process of soil softening during the initial penetration and the cyclic displacement sequences in the sensitive soil are depicted in Figure 14 that show plots of the soil structure parameter (χ). The number of cycles, denoted by N, starts from zero indicating the initial penetration followed by Episode-1 (N = 1 to 3.5) and Episode-2 (N = 4 to 5), between which soil reconsolidation was allowed. According to Figure 14, the partial softening induced during the initial penetration (N = 0) affects a region extending up to 1.5D, laterally, as measured from the centreline. The width of the fully remoulded region (blue colour) gradually increases with penetration depth because of the accumulation of remoulded soil above the T-bar due to the flow of soil around the T-bar. This soil softening caused approximately 67% decrease in soil resistance, as was shown previously in Figure 11. In the process of repeated displacement cycling, the extent of the fully remoulded region increases because the width of the failure mechanism expands with cycling. The failure mechanism as indicated by the incremental shear strains (corresponding to a vertical displacement increment of du = 0.01D) captured at the middle of the cyclic range is shown in Figure 15. The failure mechanism expands from approximately 0.84D to 0.90D during the 3.5 cycles of Episode-1 with a decreasing rate as the number of cycles increases. Accordingly, the width of the fully remoulded region within the cyclic range increases slowly as the material at the edge of the mechanism is gradually softened. The mechanism also grows in size during the subsequent cycles.

It is noteworthy that extraction and penetration of the T-bar during the cyclic sequences did not involve a cavity under or above the T-bar in this case.

The profile of normalised T-bar resistance during the cyclic sequences is depicted in Figure 16 for both episodes. It is observed that the soil resistance decreases dramatically within the early cycles (Episode-1) but then continues to reduce in an asymptotic manner with further cycling. The soil resistance decreases a further 42% at the end of Episode-1, after which the generated excess pore pressures from the preceding cycles were allowed to fully dissipate before proceeding to the second round of cycles in Episode-2.

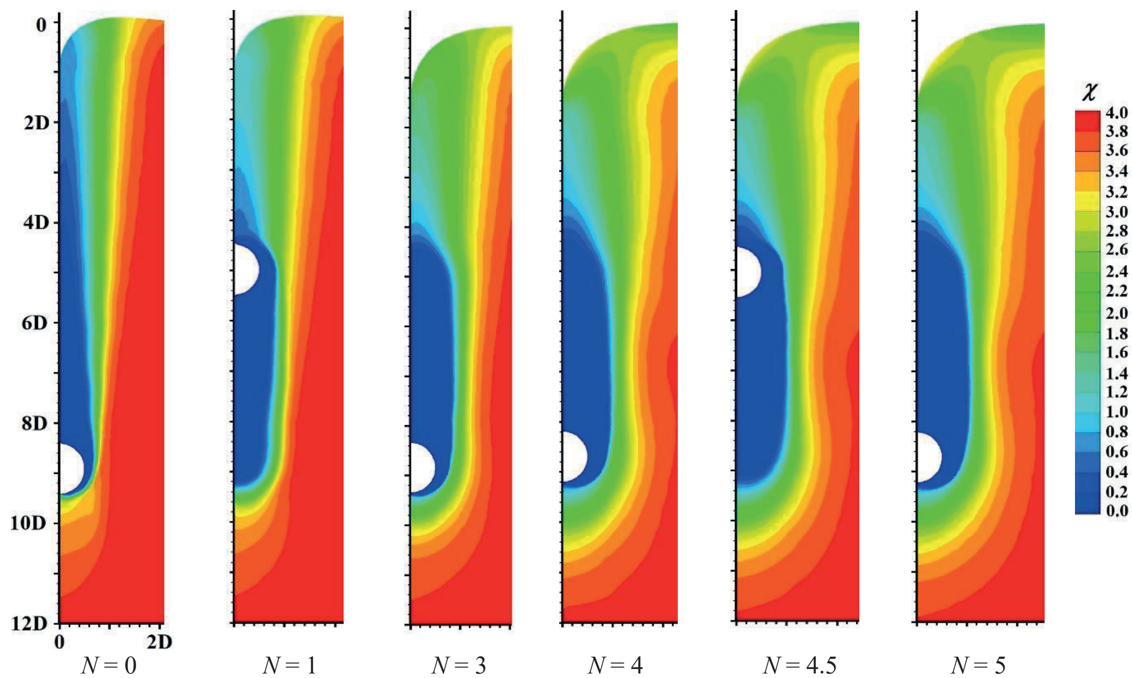

Figure 14. Soil softening during cyclic sequences: Episode-1 (cycles 1 to 3.5); Episode-2 (cycles 4 to 5)

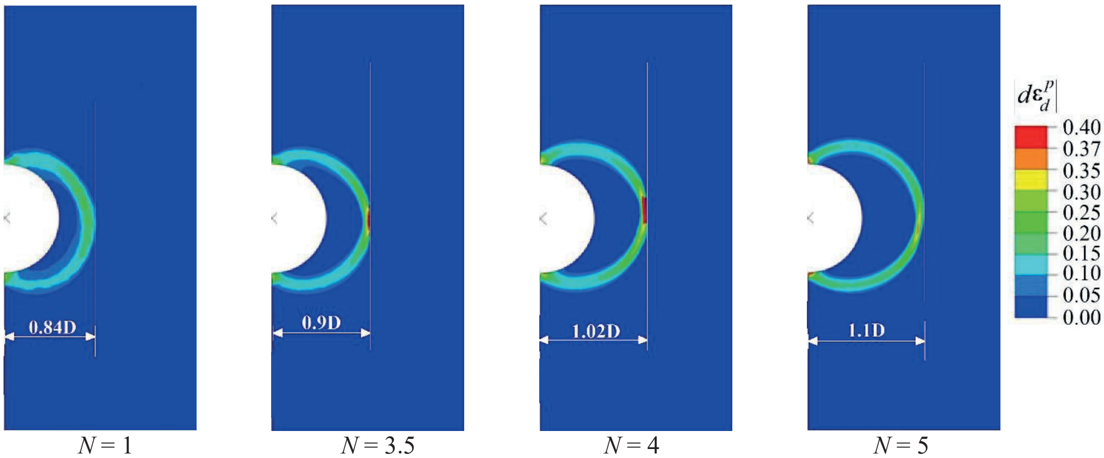

Figure 15. The width of (incremental) failure mechanism at the middle of the cyclic range ($du = 0.01D$)

Figure 16 reveals that the soil resistance increased by a factor of 1.4 upon the reconsolidation of soil. This enhanced soil resistance leads to a marked increase in the size of the failure mechanism as observed in the first cycle $N = 4$ of Episode-2 (Figures 14 & 15). The size of the failure mechanism increased by 18% during the first one and a half cycles (N = 4-5) following the soil reconsolidation, whereas it was an increase of about 7% throughout the entire cyclic sequence of Episode-1. A similar trend is then detected in Episode-2 in terms of soil strength degradation and remoulding due to cycling of the T-bar.

It is observed that the reconsolidation process has two important consequences: increasing the soil hardening parameter (as also shown in the previous example) and subsequent expansion of the failure mechanism. The latter causes further increase in the zone of influence of the loading/unloading sequences. Therefore, although the strength degrades within each episode, the regain from consolidation can be significant. Repeated phases of shearing, remoulding, and reconsolidation increase the potential for soil strength recovery. Accordingly, a ‘cyclic strength’ parameter that reflects both strength loss and strength recapture during the remoulding and reconsolidation processes should be evaluated for practical purposes.

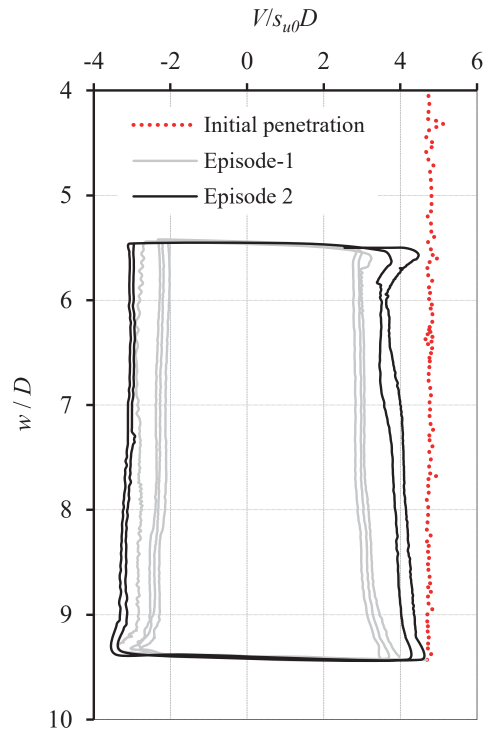

Figure 16. Profile of (normalised) soil resistance during cyclic sequences; episode 1: cyclic sequences following initial penetration; episode 2: cyclic sequences following the consolidation process (after episode 1).

Two important practical examples for which the effect of reconsolidation is increasingly being recognised and considered in design include the soil strength and axial friction beneath on-bottom pipelines (White et al., 2017) and catenary riser pipes. However, the methods to deal with them are mainly limited to approximate analytical or experimental frameworks and are usually restricted to clays of low sensitivities, whereas natural offshore clays are typically more sensitive.

Conclusion

This study has described a robust numerical tool for the analysis of a wide range of offshore geotechnical problems involving extremely large deformations and varying soil strength due to repeated loading/unloading, soil softening and reconsolidation. The numerical scheme was based on the Particle Finite Element Method (PFEM) combined with an advanced anisotropic structured constitutive soil model. The method was implemented in a commercial FE software package, Abaqus, and was successfully applied to the analysis of a pipe-seabed interaction problem and the cyclic T-bar test.

It was shown that under undrained conditions or conditions of limited pore fluid flow, shear bands are often regions of high excess pore pressures in *NC* clays. However, for heavily over-consolidated clays or dense sands, shear bands may have small excess pore pressures but this aspect was not explored in this study. Even though the localisation of excess pore pressure did not seem to be as marked as that for shear strains, such localisation could significantly change the form of the pore pressure distribution and can result in decreased consolidation times, due largely to faster drainage along the shear bands that intersect free draining surfaces. Moreover, large elastic regions were observed for highly sensitive clays as a direct consequence of intense soil softening.

The analysis of a cyclic full flow penetrometer test showed that most degradation of the soil strength occurs during the initial penetration and during the first few cycles of displacement. Reconsolidation of the soil resulted in substantial strength regain and the extent of the softened zone increased markedly due to an expanded failure mechanism. Furthermore, the capability of the numerical scheme in modelling the entire penetration process, including surface penetration, revealed the fact that soil softening upon the insertion of a T-bar causes a compact failure mechanism around the T-bar and leads to the development of a deep failure mechanism at much shallower penetration depths, whereas soils that do not soften engaged a deeper failure mechanism at a larger penetration depth and usually involve a trapped cavity above the T-bar.

The soil model used in this study considered the effects of soil structure and de-structuring. Further improvements are required to incorporate the effects of loading rate and possibly the regaining of soil structure during long-term consolidation.

References

[1] Beuth L, Więckowski Z, Vermeer PA (2011). Solution of quasi-static large-strain problems by the material point method. *Int J Numer Anal Methods Geomech* 35(13) 1451-1465.

[2] Burland JB (1990). On the compressibility and shear strength of natural clays. *Geotechnique* 40(3)329-378.

[3] Callisto L and Calabresi G (1998). Mechanical behaviour of a natural soft clay. *Geotechnique* 48(4)495-513.

[4] Chargoy CED (2014). Particle finite element methods for modelling granular material flows. PhD thesis, Univeristat Politecnica Catalunya Barcelona Tech.

[5] Chatterjee S, White DJ, Randolph MF (2013). Coupled consolidation analysis of pipe–soil interactions. *Can. Geotech. J.*, 50: 609–619.

[6] Collin F, Chambon R, Charlier R (2006). A finite element method for poro mechanical modelling of geotechnical problems using local second gradient models. *Int J Numer Meth Engng*, 65(11):1749–1772.

[7] Daflias YF, Manzari MT, Papadimitriu AG (2006). SANICLAY: simple anisotropic clay plasticity model. . *Int J Numer Anal Methods Geomech,* 30(12)1231-1257.

[8] De Borst R, Sluys LJ, Muhlhaus HB, Pamin J (1993). Fundamental issues in finite element analyses of localization of deformation. *Eng. Comput*, 10(2) 99–121.

[9] Edelsbrunner H, M EP, #252, and cke (1994). Three-dimensional alpha shapes. *ACM Trans. 681 Graph*, 13(1): 43-72.

[10] Einav I and Randolph MF (2006). Effect of strain rate on mobilized strength and thickness of curved shear bands. *Geotechnique*, 56(7)501–504.

[11] Gens A and Nova R (1993). Conceptual bases for a constitutive model for bonded soils and weak rocks. *Proc. of Int. Symp. on Hard Soils Soft Rocks*, 485-494, athens.

[12] Han Y, Yu L, Yang Q (2020). Strain softening parameters estimation of soft clay by T-bar penetrometers. *Applied Ocean Research*, 97,10294.

[13] Hodder M, White DJ, Cassidy MJ (2013). An effective stress framework for the variation in penetration resistance due to episodes of remoulding and reconsolidation. *Geotechnioque* 63(1)30-43.

[14] Hu Y and Randolph MF (1998). H-adaptive FE analysis of elastoplastic nonhomogeneous soil with large deformation. *Computers and Geotechnics*, 23(1):61–83.

[15] Idelsohn SR, Oñate E, Pin FD (2004). The particle finite element method: a powerful tool to solve incompressible flows with free-surfaces and breaking waves. *Int J Numer Methods Eng*, 61: 964-989.

[16] Karstunen M, Krenn H, Wheeler S, Koskinen M, Zentar R (2005). The effect of anisotropy and destructuration on the behaviour of murro test embankment. *Int J Geomech* (ASCE), 5(2)87-97.

[17] Leroueil S and Vaughan PR (1990). The general and congruent effects of structure in natural soils and weak rocks. *Geotechnique* 40(3)467-488.

[18] Lin H and Penumadu D (2006). Strain localization in combined axial torsional testing on Kaolin clay. *J. Eng. Mech*., 10.1061/(ASCE) 0733-9399(2006)132:5(555), 555–564

[19] Liu M, Carter JP (2002). A structured Cam Clay model. *Canadian Geotechnical Journal*, 39(6):1313-1332.

[20] Mahmoodzadeh H, Wang D, Randolph MF (2015). Interpretation of piezoball penetration in clay. *Geotechnique* 65(10)831-842.

[21] Monforte L, Arroyo M, Carbonell JM, Gens A (2018). Coupled effective stress analysis of insertion problems in geotechnics with the Particle Finite Element Method. *Computers and Geotechnics*, 101:114-129.

[22] Moore ID and Rowe RK (1988). Numerical models for evaluating progressive failure in earth structures—A review. *Comput. Geotech*, 6(3)217–239.

[23] Nazem M, Carter JP, Airey DW, Chow SH (2012). Dynamic analysis of a smooth penetrometer free-falling into uniform clay. *Geotechnique*, 62(10)893–905.

[24] Nazem M, Sheng D, Carter JP (2006). Stress integration and mesh refinement in numerical solutions to large deformations in geomechanics. *Int J Numer Methods Eng*, 65:1002–1027.

[25] O'Loughlin CD, Zhou Z, Stainer SA, White DJ (2020). Load-controled cyclic T-bar tests: a new method to assess effects of cyclic loading and consolidation. *Geotechnique Letters* 10:7-15.

[26] Peuchen J and Terwindt J (2016). Critical appraisal of T-bar penetration tests. *Geotechnical and Geophysical Site Characterisation*. Lehane, Acosta-Martínez & Kelly (Eds) @ 2016 Australian Geomechanics Society, Sydney, Australia, ISBN 978-0-9946261-1-0.

[27] Rangi R, Wang D, Masin D, Bienen B, Cassidy M, Stainer S (2016). Numerical modelling of the effects of consolidation on jack-up spudcan penetration. *Computers and Geotechnics* 78:25-37.

[28] Rodriguez JM, Carbonell JM, Cante JC, Oliver J. The particle finite element method (PFEM) in thermo- mechanical problems. *Int J Numer Meth Eng*, 107(9)733-785.

[29] Sabetamal H, Carter JP, Nazem M, Sloan SW (2016). Coupled analysis of dynamically penetrating anchors. *Computers and Geotechnics*, 77:26-44.

[30] Sabetamal H, Carter JP, Sloan SW (2018). Pore pressure response to dynamically penetrating anchors. *Int. J. Geomechanics*, 18(7)04018061-1-16.

[31] Sheng D, Sloan SW, Yu H. (2000). Aspects of finite element implementation of critical state models. *Computational Mechanics*, 26:185-196.

[32] Shuttle DA and Smith IM (1990). Localization in the Presence of Excess Pore water Pressure. *Computers and Geotechnics* 9:87-89.

[33] Sloan SW, Abbo A, Sheng D (2001). Refined explicit integration of elastoplastic models with automatic error control. *Engineering Computations*, 18:121-154.

[34] Smith PR, Jardine RJ, Hight DW (1992). On the yielding of Bothkennar clay. *Geotechnique*, 42(2)257-274.

[35] Soga K, Alonso E, Yerro A, Kumar K, Bandara S (2016). Trends in large-deformation analysis of landslide mass movements with particular emphasis on the material point method. *Geotechnique,* 66(3)248-273.

[36] Stewart DP (1992). Lateral loading of piled bridge abutments due to embankment construction. Ph.D. thesis, The University of Western Australia.

[37] Stewart DP and Randolph MF (1994). T-Bar penetration testing in soft clay. *J. Geotech. Engng*, ASCE 120(12) 2230–2235.

[38] Sulsky D, Zhou S, Schreyer HL (1995). Application of a particle-in-cell method to solid mechanics. *Computer Physics Communications* 87, 235-252.

[39] Susila E, Hryciw RD (2003). Large displacement FEM modelling of the cone penetration test (CPT) in normally consolidated sand. *Int J Numer Anal Methods Geomech*, 27(7) 585-602.

[40] Taiebat M, Dafalias YF, Peek R (2010). A destructuration theory and its application to SANICLAY model. *Int J Numer Meth Eng*, 34(10), 1009-1040.

[41] Thakur V, Nordal S, Viggiani G, Charrier P (2018). Shear bands in undrained plane strain compression of Norwegian quick clays. *Can. Geotech. J*., 55(1).

[42] Tho KK, Leung CF, Y. Chow YK, Palmer AC (2011). Deep cavity flow mechanism of pipe penetration in clay. *Can. Geotech. J*. 49 (1): 59–69.

[43] van den Berg P, deBorst R, Huetink H (1996). An Eulerian finite element model for penetration in layered soil. *Int J Numer Anal Methods Geomech*, 20(12) 865-886.

[44] Wang D and Bienen B (2016). Numerical investigation of penetration of a large-diameter footing into normally consolidated kaolin clay with a consolidation phase. *Geotechnique*, 66(11)947-952.

[45] Wang D, Bienen B, Nazem M, Tian Y, Zheng, J, Pucker T, Randolph MF (2015). Large deformation finite element analyses in geotechnical engineering. *Computers and Geotechnics*, 65:104-114.

[46] Wang Y, Hu Y, Hossain MS, Zhou M. (2020). Effect of Trapped Cavity Mechanism on Interpretation of T-Bar Penetrometer Data in Uniform Clay. *J. Geotech. Geoenviron. Eng*, 146(9):04020078.

[47] Wheeler, S., Naataanen A. Karstunen M, Lojander M (2003). An anisotropic elasto-plastic model for soft clays. *Can. Geotech. J*., 40:403-418.

[48] White DJ, Clukey EC, Randolph MF, Boylan NP, Bransby MF, Zakeri A, Hill AJ, Jaeck C (2017). The state of knowledge of pipe-soil interaction for on-bottom pipeline design. *In Proceedings of the Offshore Technology Conference (OTC)* 2017, vol. 2, pp. 969–995, Houston, TX, USA: Offshore Technology Conference.

[49] White DJ, Gaudin C, Boylan N, Zhou H (2010). Interpretation of T-bar penetrometer tests at shallow embedment and in very soft soils. *Can. Geotech. J*. 47 (2): 218–229.

[50] Wroth, C.P. 1984. The interpretation of in situ soil tests. *Géotechnique*, 34(4):449–489. doi:10.1680/geot.1984.34.4.449.

[51] Yafrate N, Dejong J, Degroot D, Randolph MF (2009). Evaluation of remolded shear strength and sensitivity of soft clay using full-flow penetrometers. *J. Geotech. Geoenviron. Engng* 135(9)1179–1189.

[52] Yang C, Carter JP, Sheng D, Sloan SW (2016). An isotach elastoplastic constitutive model for natural soft clays. *Computers and Geotechnics*, 77:134-155.

[53] Yi JT, Goh SH, Lee FH, Randolph MF (2012). A numerical study of cone penetration in fine-grained soils allowing for consolidation effects. Geotechnique, 62(8)707-719.

[54] Yin ZY, Chang CS, Karstunen M, Hicher PY (2010). An anisotropic elastic–viscoplastic model for soft clays. *Int J Solids Struct*, 47:665-677.

[55] Zhang X, Krabbenhoft K, Pedroso DM, Lyamin AV, Sheng D, da Silva MV, Wang D (2013). Particle finite element analysis of large deformation and granular flow problems. *Computers and Geotechnics*, 54:133-142.

[56] Zhang X, Oñate E, Andres S, Torres G, Bleyer J, Krabbenhoft K. (2019). A unified Lagrangian formulation for solid and fluid dynamics and its possibility for modelling submarine landslides and their consequences. *Comput. Methods in Appl. Mech. Eng,* 343:314-338.

[57] Zhou Z, Randolph MF (2009) Numerical investigations into cycling of full-flow penetrometers in soft clay. (2009). *Geotechnique* 59(10)801–812.

[58] Zhou Z, White DJ, O'Loughlin CD (2019). An effective stress framework for estimating penetration resistance accounting for changes in soil strength from maintained load, remoulding and reconsolidation. *Geotechnique* 69(10)57-71.

[59] Zhu B, Dai J, Kong D (2020) Modelling T-bar penetration in soft clay using large displacement sequential limit analysis. *Geotechnique* 70(2)173-180.

[60] Zienkiewicz OC and Taylor RL (2000). The Finite element method: Vol 2, Solid mechanics, Butterworth-Heinemann, Woburn, MA.

[61] Zienkiewicz OC, Zhu JZ (1992). The superconvergent patch recovery and a posteriori error estimates. Part 1: the recovery technique. *Int J Numer Meth Eng*, 33:1331–1364.